International Journal of Multiphase Flow 174 (2024) 104786

Contents lists available at ScienceDirect

International Journal of Multiphase Flow

journal homepage: www.elsevier.com/locate/ijmulflow

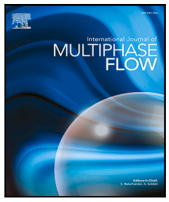

Effect of inflow disturbances in Pelton turbine distributor lines on the water jet quality

Bernhard Semlitsch

TU Wien, Getreidemarkt 9/BA, Vienna 1060, Austria

ARTICLE INFO

Keywords:
Pelton turbine efficiency
Water jet quality
Inflow perturbations
Flow energy losses
Numerical flow simulation
Multiphase flow

ABSTRACT

The proper design of the manifold, distributing the flow to the individual nozzles, is crucial for the Pelton turbine performance. The generation of both energy losses and secondary flows must be reduced to a minimum to provide optimal water jet quality and, hence, efficiency. However, the inflow state due to the penstock is commonly disregarded at the design stage. By numerical flow simulation, we show how such penstock perturbations affect the water jet cross-section and axis deviation by considering different pipe bends upstream of the manifold. The two-phase flows resulting in a typical Pelton turbine manifold are predicted using the Volume-Of-Fluid (VOF) approach in conjunction with the $k-\omega$ SST turbulence closure model. Pipe bends are attached five manifold inlet diameters upstream of the manifold itself. The consequences on the secondary flows in the nozzles and the free water jet quality are reported quantitatively. The analysis shows that even small inflow perturbations into the manifold due to penstock piping significantly affect the water jet quality. A yet unreported mechanism is revealed, where the secondary flows mitigate the impact of the flow rate imbalance across the nozzle on the water jet deviation.

1. Introduction

Pelton turbines are employed for electricity generation at low water flow rates and high heads (Giesecke and Mosonyi, 2009). The water is guided via the penstock pipes from the high-altitude reservoir to the turbine. The potential energy is converted into kinetic energy by forming a free jet at the end of the pressure line. Impinging onto the buckets, the impulse of the water jet rotates the Pelton turbine runner, which transfers the rotational energy over the shaft to the electric generator.

The distributor line or manifold is the piping segment prior to the nozzles, which divides the flow equally. In this process, the energy losses must not exceed 2%–3% of the total water head. Moreover, the secondary flows, induced by flow separation at abrupt bends and internal installations, disperse and deviate the free jet (Zhang and Casey, 2007; Staubli et al., 2009). Thereby, losses are generated at the runner (Santolin et al., 2009; Kumashiro et al., 2019). Wide cross-sections and large curvature radii at pipe bifurcations are desired to mitigate flow separation but increase the frictional losses, the weight, and hence, the cost of the distributor line, including housing. Thus, these design criteria have to be balanced.

Computational simulations aid the design of the distributor line by assessing the energy losses and the jet flow quality (Mack et al., 2006; Han et al., 2019). Even post-processing techniques have been developed to visualise the vortical structure generation in the manifold (Sadlo et al., 2004). The turbulent, two-phase flow demands modelling to enable fast performance predictions to screen numerous scenarios. Whereas the volume-of-fluid method has become standard to replicate the interface between water and air in Pelton turbine applications (Sandmaier et al., 2023), various turbulence closures have been applied (Hahn et al., 2022). The $k-\omega$ SST (Chongji et al., 2016; Jošt et al., 2019), the $k-\epsilon$ (Patel et al., 2010), and the $k-\epsilon$ RNG (Han et al., 2019) closure model have been employed in literature.

Pipe bends affect the free water jet deformation crucially, e.g. shown by Zhang and Casey (2007) assessing the water jet deformation due to a 90° pipe bend experimentally. The Dean vortex forming in pipe bends generally governs the secondary flow structure and the free water jet shape. Fiereder et al. (2010) showed that computational flow simulations can consistently capture such water jet deformations with experiments. Many numerical studies were conducted to predict such water jet deformations in complex distributor line applications. Staubli et al. (2009) revealed that the secondary flow amplitudes in water jets can reach up to 3% of the axial flow velocity. Peron et al. (2008) and Mack et al. (2014) showed numerically how inserts in the needle holder can reduce the free water jet dispersion and thereby mitigate the cavitation and noise problems of the power plant. Santolin et al. (2009), Jošt et al. (2010), Zeng et al. (2018), and Kumashiro et al. (2019) included a part of the penstock and the runner in their numerical simulations to show how it affects the Pelton turbine efficiency. By including all components from the penstock to the Pelton

E-mail address: bernhard.semlitsch@tuwien.ac.at.

https://doi.org/10.1016/j.ijmultiphaseflow.2024.104786
Received 27 October 2023; Received in revised form 22 February 2024; Accepted 25 February 2024
Available online 28 February 2024

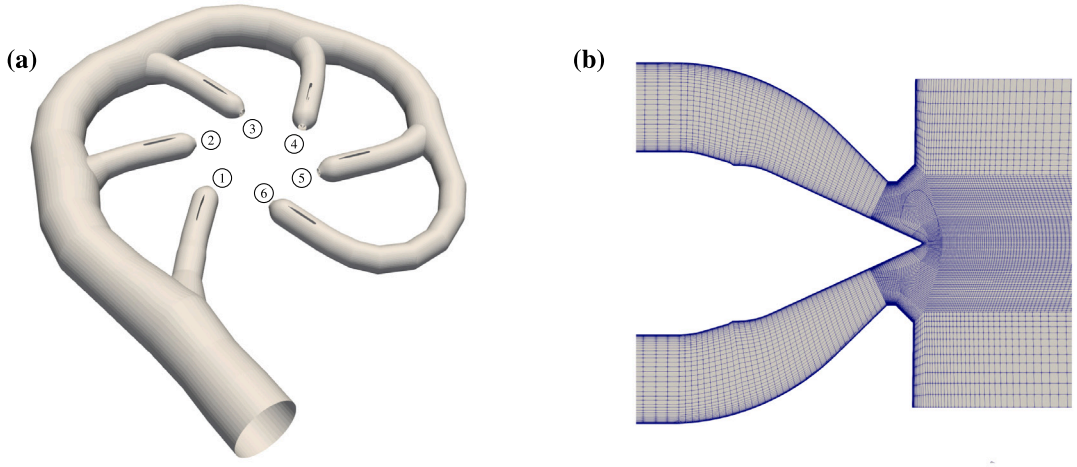

Fig. 1. The geometry of the investigated distributor is shown in (a), where the nozzle numbering is indicated. A zoomed detail shown in (b) illustrates the application of hanging-node mesh refinement in a horizontal cut-plane at one nozzle exit.

turbine runner in the distributor line optimisation process, the computational simulations become costly. A better comprehension of flow phenomena affecting the free water jet quality and characterisation by criteria would allow the reduction of the optimisation domain.

Hence, a lack of understanding of the factors influencing the water jet quality in Pelton turbine manifolds with multiple nozzles can be identified. We show how the free water jet quality is affected in the distributor line by typical penstock perturbations. By attaching different pipe bends five manifold inlet diameters upstream of the manifold, inflow scenarios are created, and the quality of the numerically simulated water jets is quantified. By correlating the free water jet quality parameters with the flow upstream of the nozzle, the important influence factors are identified. Thereby, an unreported interaction mechanism between the secondary flows and the mass flow rate imbalance across the nozzle is unravelled.

2. Methodology and setup

The investigated distributor geometry with six nozzles is shown in Fig. 1(a). The nozzles are equipped with an internally regulated spear valve vertically held by hydrofoil-shaped profiles. The non-dimensional spear valve opening ratio s/d_0 is 0.79, where s is the needle valve retracting position and d_0 is the nozzle orifice diameter. The flow is driven by the head, which is specified in terms of the total pressure, $p_0 = \varrho_{water}\mathbf{g}h$ where $h = 80$ m, at the inlet. The manifold inlet diameter is 0.33 m. The static pressure is set to standard atmospheric conditions at the outlet, where free-stream entrainment boundary conditions are specified. The properties applied for water are the density, $\varrho_{water} = 1000$ kg/m^3, and the kinematic viscosity, $\nu_{water} = 1 \cdot 10^{-6}$ m^2/s, and the properties for air are the density, $\varrho_{air} = 1$ kg/m^3, and the kinematic viscosity, $\nu_{air} = 1.48 \cdot 10^{-5}$ m^2/s.

The effect of perturbations generated upstream of the distributor is studied by attaching different penstock segments, i.e. pipe bends. The inlet pipe is extended by five times the manifold inlet diameter, where pipe bends from −90° to 90° are attached at a step-size of 30° with a curvature radius of two times the manifold inlet diameter. Another pipe extension of five times the manifold inlet diameter is placed upstream of the bends to ensure undisturbed flow development. A cylindrical domain is attached downstream of the nozzle exit to investigate the free water jet development, which has a diameter and a length of five and ten times the nozzle exit diameter, respectively.

The three-dimensional Navier–Stokes equations are solved numerically using OpenFOAM v2206 to simulate the two-phase flow using the Volume-Of-Fluid (VOF) method. The density, ϱ, and the dynamic viscosity, μ, are formed proportionally to the volume fraction of the fluids contained in a cell volume,

$$\varrho = \alpha\,\varrho_1 + (1-\alpha)\,\varrho_2 \qquad \text{and} \qquad \mu = \alpha\,\mu_1 + (1-\alpha)\,\mu_2\,, \tag{1}$$

where $\alpha = 1$ if the fluid 1, i.e. water, fills entirely the volume and $\alpha = 0$ if only the fluid 2, i.e. air, fills the volume. The volume fraction distribution, α, is tracked by the transport equation

$$\frac{\partial \alpha}{\partial t} + \nabla \cdot (\mathbf{u}\,\alpha) + \nabla \cdot (\mathbf{u}_r\,\alpha(1-\alpha)) = 0\,, \tag{2}$$

where t is the time and $\mathbf{u}$ is the flow speed. The relative velocity, $\mathbf{u}_r = \mathbf{u}_1 - \mathbf{u}_2$, between the phase velocities is modelled by the speed, $\mathbf{u}_c$, employing the interface compression method,

$$\mathbf{u}_c = \min(C_\alpha \mathbf{u}, \max(|\mathbf{u}|))\frac{\nabla\alpha}{|\nabla\alpha|}\,, \text{ where} \qquad C_\alpha = 1. \tag{3}$$

The mass conservation equation

$$\frac{\partial \varrho}{\partial t} + \nabla \cdot (\varrho\,\mathbf{u}) = 0 \tag{4}$$

and the momentum conservation equations

$$\frac{\partial(\varrho\,\mathbf{u})}{\partial t} + \nabla \cdot (\varrho\,\mathbf{u}\mathbf{u}) = -\nabla p + \nabla \cdot \mu(\nabla\mathbf{u} + \nabla\mathbf{u}^T) + \mathbf{f}_\sigma \tag{5}$$

are numerically computed to represent the flow behaviour, where p is the pressure and $\mathbf{f}_\sigma$ represents the surface tension source term. Surface tension between the two fluids is accounted for by the formula,

$$\mathrm{f}_{\sigma,j} = \sigma\kappa\,\frac{\partial\alpha}{\partial x_j}\,, \text{ where} \qquad \kappa = -\nabla\cdot\mathbf{n} = -\nabla\cdot\left(\frac{\nabla\alpha}{|\nabla\alpha|}\right)\,, \tag{6}$$

σ represents the surface tension constant with the value 0.07 N/m and κ is the surface curvature. The interface normal vector, $\mathbf{n}$, is estimated by calculating the normalised gradient of the volume fraction, α.

The manifold flow is assumed to be turbulent due to the high Reynolds number (based on the manifold inlet diameter and mean velocity). Moreover, steady-state flow solutions are sought, and thus, the Reynolds-Averaged Navier–Stokes equations are solved. The $k-\omega$ SST closure is employed to model the turbulent flow behaviour. Being a blend of the $k-\varepsilon$ and the $k-\omega$ model, the $k-\omega$ SST model combines the advantages of being able to resolve wall-bounded flows and robustness to small turbulence boundary condition variations. A turbulence intensity of 5% is set at the inlet, with the hydraulic diameter being the turbulent mixing length scale.

The Flux-Corrected Transport (FCT) method is employed to compute the volume fraction advection equation, where the Multidimensional Universal Limiter for Explicit Solutions (MULES) approach is used to maintain a sharp and bounded phase interface. The *pimple* algorithm, a

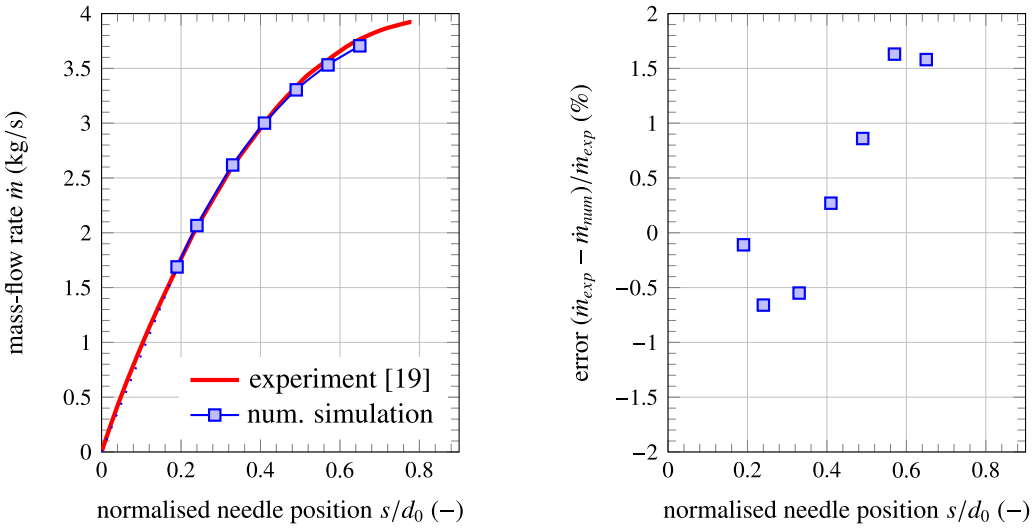

Fig. 2. Comparison of the operating curve for a single nozzle obtained by Unterberger et al. (2010) with numerical predictions applying the presented methodology.

combination of the *simple* and *piso* algorithms, is used for the pressure–velocity coupling, where the pressure correction equation and the non-orthogonal correction is updated three times for each outer iteration. The local Euler time-stepping scheme has been used to compute the steady-state flow solutions, where the cell-based pseudo-time-step size has been limited to a Courant number of 0.2. The gradients are calculated using a cell value-limited least squares integration scheme. The divergence term in the volume fraction transport equation is discretised with the Van Leer limited Gauss scheme. All other divergence operations are discretised with a second-order upwind scheme. All Laplace operations are solved with a linear Gaussian scheme.

The numerical domains are discretised by fully structured grids, as shown in Fig. 1(b). Refinements have been applied towards all walls to ensure $y^+ \leq 5$, where large values occur only at the nozzle exit and $y^+ < 1$ in the rest of the domain. This guarantees that flow separations are resolved as well as possible. A hanging-node refinement has been employed in the free-stream core region to capture the free water jet surface. The total cell counts are approximately 31.84 million for each individual mesh. A grid sensitivity study was performed by Hahn et al. (2022), where the finest mesh with refinements was considered in this study. However, no grid convergence study was carried out for the entire computational domains with pipe bends.

The numerical methodology is validated against experimental measurement data by Unterberger et al. (2010), where the "sharp" single nozzle configuration has been chosen due to the similarity with the nozzle geometry considered in this investigation. The computational flow simulations have been conducted with the same meshing strategy and numerical setup as presented above. The boundary condition values are set to replicate the operating conditions specified by Unterberger et al. (2010), i.e. the acting head of the upper reservoir was set as the inflow boundary condition and the standard atmospheric conditions at the outlets. Fig. 2 reveals excellent agreement (below 1.7% difference) between the numerical and experimental data showing the nozzle operating curve.

3. Results

Fig. 3 shows the general velocity magnitude distribution for different pipe bend configurations upstream of the Pelton turbine manifold. Downstream of the penstock bends, the bulk flow deviates off the pipe walls causing an uneven velocity distribution entering over the cross-section manifold inlet. The penstock pipe bend wake, i.e. visible as lower velocity magnitudes on the pipe bend side, remains notable until the manifold inlet. The heading direction of the high momentum flow[1] continues at an angle compared to the design inflow direction, which decisively alters the internal manifold flow.

The high momentum flow is pushed radially outwards in the manifold for penstock pipe bend configurations with negative angles, i.e. −90°, −60°, and −30°. Thus, lower momentum flow reaches the first nozzle. On the contrary, the high momentum flow is directed onto the first nozzle for positively angled penstock pipe bends. The particular angle of the high momentum flow at the manifold inlet heads onto particular nozzles. For example, the configuration with a −30° pipe bend causes high velocities at the deviation of the second branch line. Higher velocities are visible at the deviation of the third, fourth, and fifth branch lines for positive pipe bend angles. While significant differences in the velocity magnitude can be observed until the fourth and fifth branch lines, only minor impact is notable in the sixth branch line.

The flow features at the nozzle exit define the free water jet shape. The velocities are illustrated in Fig. 4 on planes just upstream of the central needle bodies, where their locations are illustrated in Fig. 3. The central needle bodies reach into the curved branch lines because of the tight packing constraints. Therefore, the velocity contours shown in Fig. 4 reveal the impact of the downstream located blockage. Clearly, all images exhibit lower primary and higher secondary velocities in the centre.

Fig. 4 reveals the impact of the branch line curvature for all cross-sections. The primary velocity is higher at the outer radii, while low primary flow velocities are notable at the inner radii due to vortex pair generation. Low primary velocities due to wake formation can be noted in the second and third branch lines but also in other higher-numbered branch lines.

The in-plane or secondary velocity magnitude appears low for the first and high for the second branch line. With positive penstock pipe bend angles, the secondary velocity magnitudes are even higher for the third branch line. The secondary velocity magnitude appears similar for higher-numbered branch lines. An amplification of secondary velocity magnitudes can be noted when high momentum flow occurs at the inner radii and causes flow separation at the branch line junction.

The free water jet shapes are qualitatively illustrated in Fig. 5 by iso-surfaces of the air/water interface. The best water jet cross-sections can

[1] With the pipe bend, the flow is pushed towards the outer pipe walls. The flow remains to exhibit high-velocity magnitudes at the opposite side of the pipe bend, even five pipe diameters downstream.

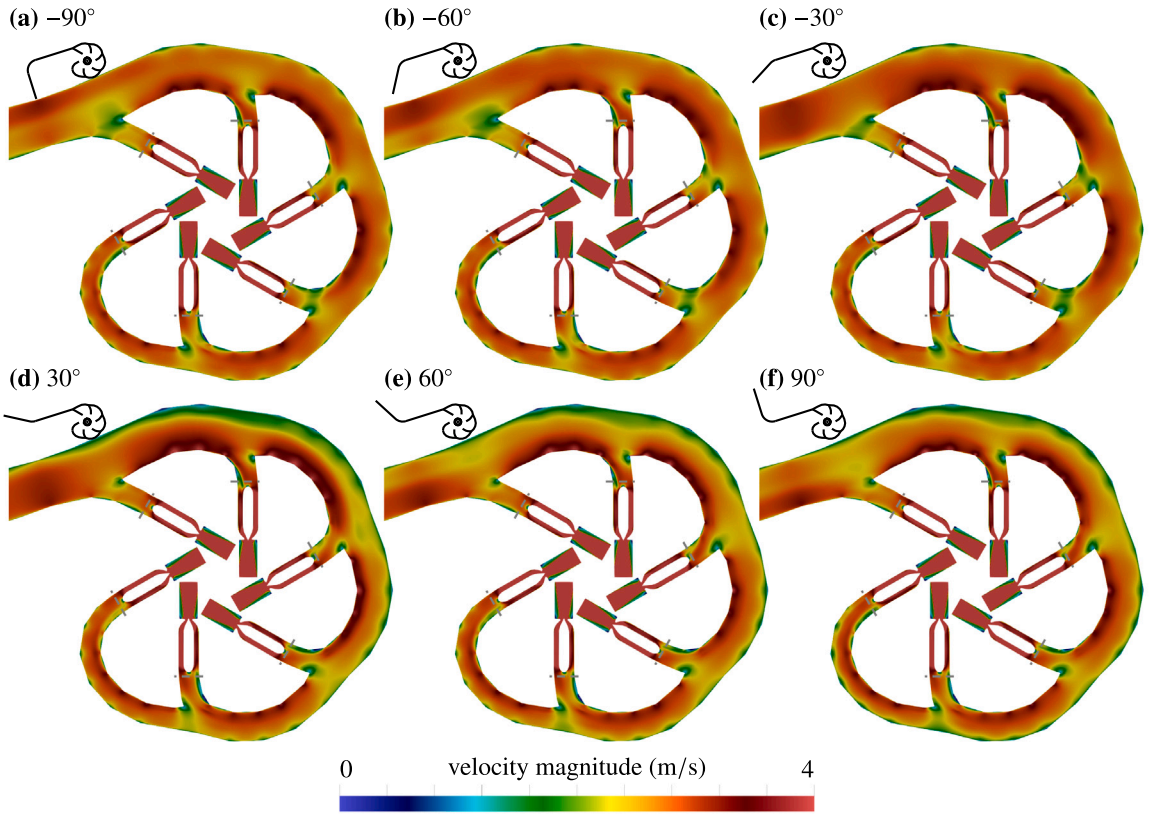

Fig. 3. The velocity magnitude contours in the mid-plane view are shown for different penstock pipe bend configurations. (Grey dashed lines indicate the plane locations of Fig. 4.) (For interpretation of the references to colour in this figure legend, the reader is referred to the web version of this article.)

be observed for the first nozzle, as expected from the observations of the velocities upstream of the needle body. Depending on the upstream pipe bend configuration, the worst water jet cross-sections can be observed for the second or third manifold nozzle. A nose arises, similarly as described by Riemann (2009) or Zhang and Casey (2007), due to the secondary flows for these water jets. Noteworthy is that several shapes of the water jets are similar, although the secondary velocities shown in Fig. 4 exhibit significant differences. Thus, establishing a direct relation between secondary flow velocities upstream of the needle body and the water jet shape is challenging.

The quality of the water jet shapes can be quantified by several criteria, i.e. water jet circularity and water jet deviation. The water jet deviation is defined as the angular difference of the water jet centreline compared to the ideal or needle axis (Staubli et al., 2009). The description of the water jet deviation as an angle challenges the evaluation procedure because of the required origin definition. Given that changes in the water jet deviation angle along the water jet axis require a force interaction, the assumption of the nozzle exit (or slightly downstream due to the spear) as a fixed-point origin seems reasonable. Fig. 6 shows that the water jet deviation[2] off the ideal axis starts indeed approximately from the nozzle exit and evolves linearly with the increasing distance. The estimation with the nozzle exit as origin corresponds to a maximal and minimal deviation angle of 0.32° and 0.17°, respectively. Even such small water jet deviation angles might affect the Pelton turbine performance significantly (Deng et al., 2023).

Irrespective of the pipe bend configuration, the water jet deviation of the fifth nozzle is the largest, and the water jet deviation is the lowest with the first and third nozzle.

The cross-sectional deformation of water jets can be quantified by their perimeter evolution along the axis, which is plotted as a ratio to the equivalent circumference enclosing the same area in the lower row of Fig. 7. The water jet perimeter increases continuously with the axial distance from the nozzle exit. The water jet emerging from the first nozzle exhibits the smallest perimeter for most pipe bend configurations, while the water jet originating from the second nozzle has the largest perimeter for all pipe bend configurations. The water jets from the third nozzle also exhibit a similarly large perimeter for the penstock pipe bend configurations with a positive angle.

The circularity or out-of-roundness parameter estimates the cross-sectional water jet deformation by a simpler relation, which is defined as the difference between the maximal and minimal diameter of the water jet divided by theoretical diameter (Staubli and Bissel, 2009). Because the water jet is generally not elliptic nor axisymmetric with respect to the semi-major axis (and therefore, the measure as diameter differences over the centreline might obfuscate water jet deformations), we prefer the definition via the radii to the calculated water jet centreline, i.e. $c_\circ = r_{\max} - r_{\min}/r_{\text{theoretical}}$. The upper row in Fig. 7 shows the evolution of the out-of-roundness parameter over the axial distance. At the nozzle opening configuration considered, the needle reaches out through the nozzle exit plane. The impact can be noted as a small axial offset before the out-of-roundness parameter starts to rise. The out-of-roundness parameter increases linearly until an axial distance of approximately two nozzle exit diameters downstream of the nozzle. Thereafter, the growth rate reduces and flattens off. Comparing the rows in Fig. 7 reveals that the two parameters rank the water jet quality

[2] The deviation has been calculated in each plane by summing over the area-weighted water contained cells multiplied by the distance to the reference and dividing by the total water contained area, i.e. $\Delta = \sum_i(\alpha A_{\text{cell},i} \cdot (y_i - y_{\text{ref}}))/\sum_i(\alpha A_{\text{cell},i})$.

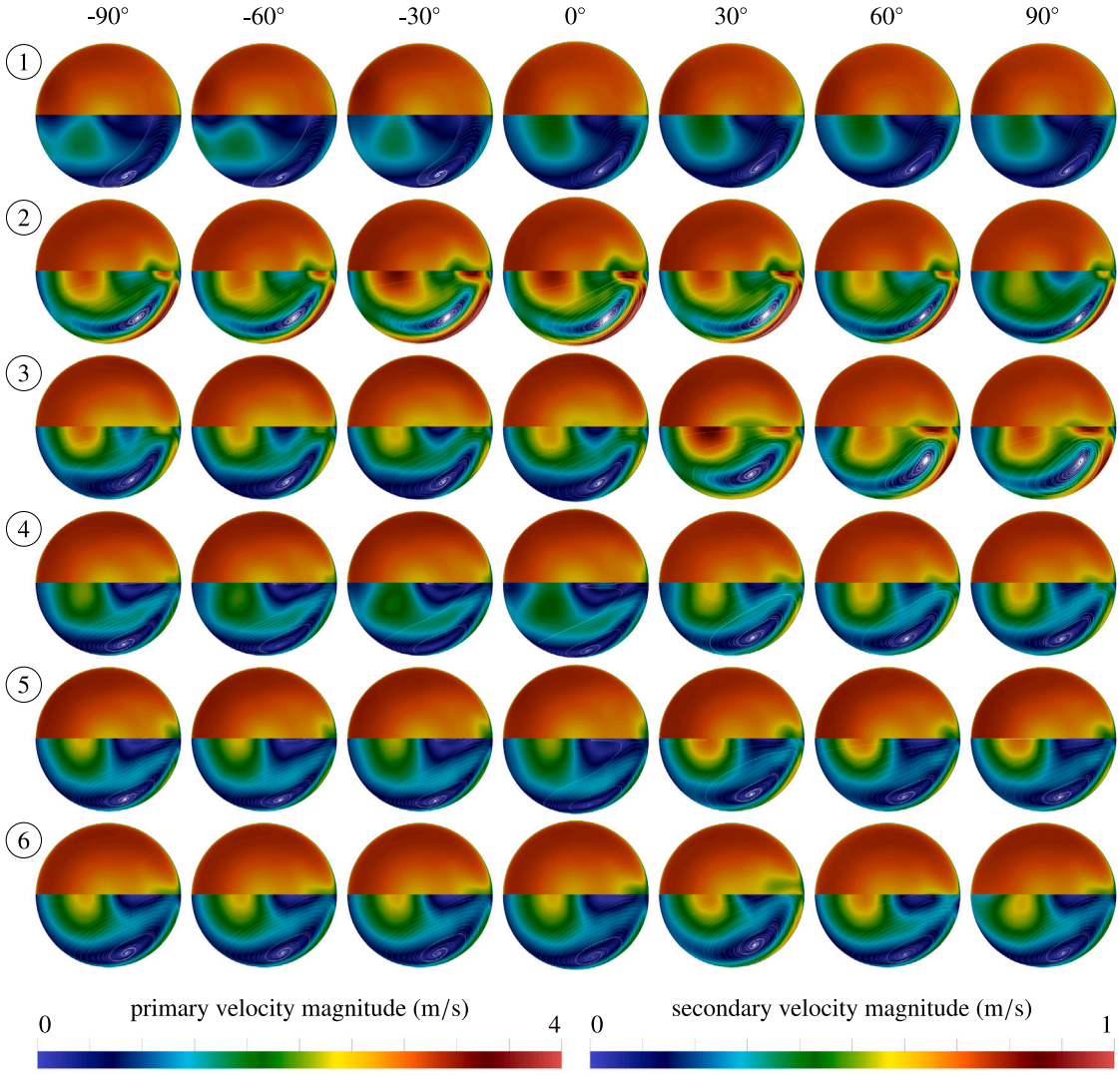

Fig. 4. The primary and secondary velocities are shown on planes just upstream of the needle bodies (the locations are indicated in Fig. 3, and the reader looks towards the nozzle exit). The primary velocity magnitude, $\|u_{\text{pri}}\| = \mathbf{u} \cdot \mathbf{n}$ (where $\mathbf{n}$ is the plane unit normal vector), is shown on the upper half, while the secondary velocity magnitude, $\|u_{\text{sec}}\| = \|\mathbf{u} - (\mathbf{u} \cdot \mathbf{n}) \cdot \mathbf{n}\|$, is plotted on the lower half.

in terms of cross-sectional deformation consistently, but the progression over the axial distance to the nozzle exit is different.[3]

The side imbalance of the mass flow rate and the secondary velocity ratio in the nozzle are commonly used as estimates to predict the water jet quality. Fig. 4 showed that the primary flow velocities are unequal on each side of the vertical profiles supporting the needle body. The percentual excess of the mass flow rate on the outer side compared to the ideal equal distribution is tabulated in Table 1.[4] The highest side imbalance of the mass flow rate occurs for the second and the fifth nozzle, whereas the mass flow rates at each side of the nozzle are almost equal for the first nozzle. Comparing the results for the side imbalance of the mass flow rate with the water jet deviation plotted in Fig. 6 reveals some similarities, e.g. that the fifth nozzle with high side imbalance has a high water jet deviation and that the first nozzle with low side imbalance has a low water jet deviation. Nonetheless, the highest values of the side imbalance occur for the second nozzle, which does not exhibit the highest water jet deviation.

The secondary velocity magnitudes normalised by the primary flow velocity for the station upstream of the needle body are listed in Table 2.[5] Clearly, high secondary velocity magnitudes occur for the second and third nozzles, where the highest obtained values for each pipe bend configuration depend on the pipe bend angle. Comparing the tabulated results for the secondary velocity magnitude ratio with the normalised perimeter shown in Fig. 7 indicates that the secondary velocity magnitude ratio is a good estimator for the water jet deformation but inaccurate on some occasions. For positive pipe bend angles, i.e. 60° and 90°, the highest secondary velocity magnitude ratios are obtained for the third nozzle, whereas Fig. 7 shows that the largest water jet deformation occurs at the second nozzle. Further, the ranking between

[3] The out-of-roundness parameter is expected to be less suited for complex deformed water jets, such as shown by Staubli et al. (2009).

[4] Ideally, the mass flow rates are equal, i.e. 50%, at both sides of the vertical support profile. The percentual imbalance of the mass flow rates is calculated as $((\dot{m}_l/(\dot{m}_l + \dot{m}_r)) - 0.5) \cdot 100$, where the index l and r indicate the left and the right side of the vertical support profile in the view direction towards the Pelton turbine runner.

[5] Secondary velocity ratios have been used in different forms, i.e. area-averaged, mass-flow-averaged, or flux-weighted, in literature. All forms have been evaluated and compared. The values and relative proportions change, but the general relative ranking is conserved. Hence, the form of secondary velocity ratio evaluation does not change the conclusions drawn in this work.

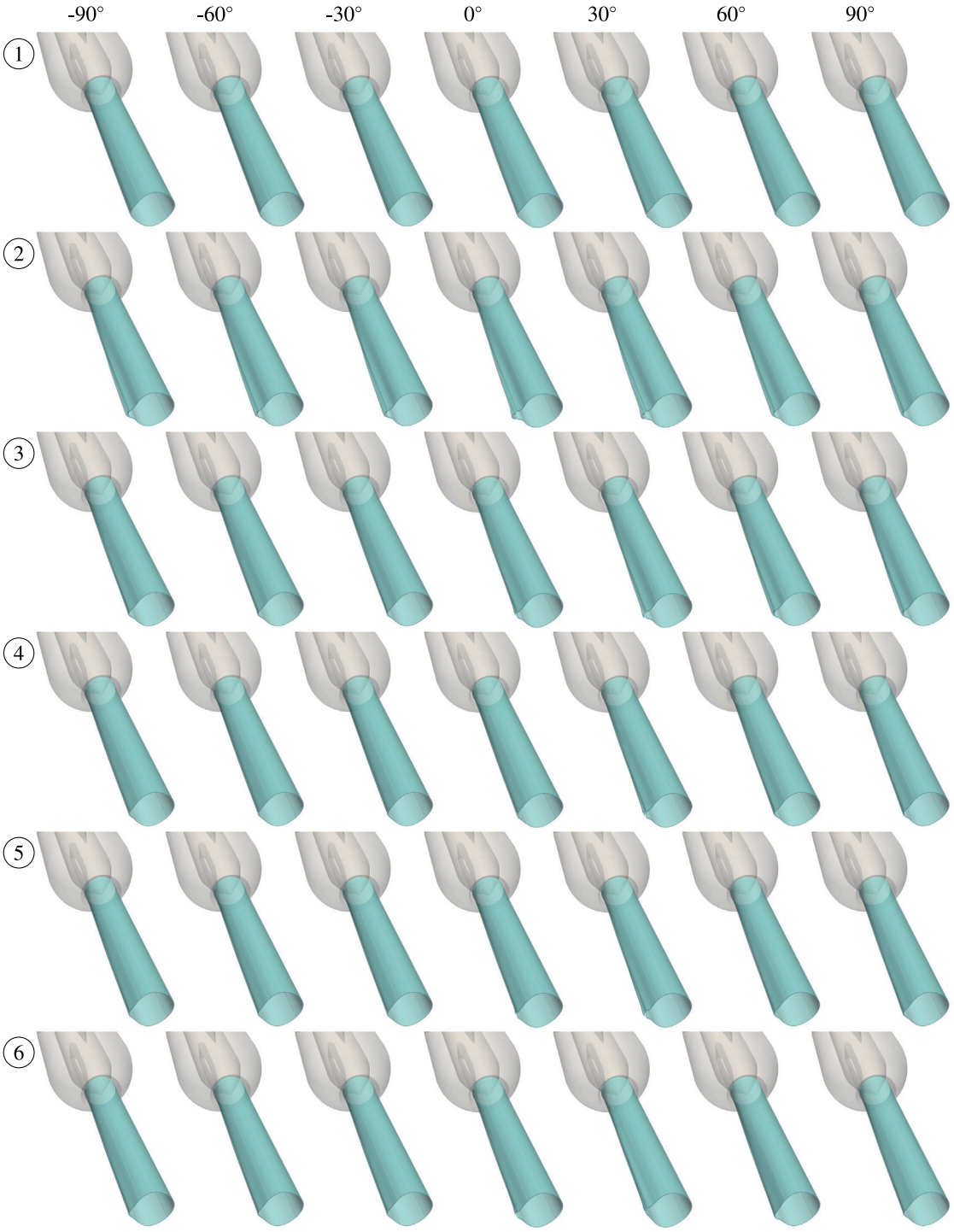

Fig. 5. The shapes of the free water jets are illustrated by iso-surfaces (with the value of 0.2) of the air/water interface as a function of penstock pipe bend configuration and nozzle number. The airfoil-shaped profiles hold the needle body vertically, and the curved branch lines feed the nozzle from the left.

Table 1
The side imbalance of the mass flow rate at the nozzles mid are listed in percent for different penstock pipe bend configurations.

	−90°	−60°	−30°	0°	30°	60°	90°
①	0.6684	0.6777	0.9400	0.7866	0.8818	0.8558	0.7640
②	1.6529	1.6577	1.9901	1.9702	1.9141	1.5938	1.3734
③	1.2254	1.1818	1.1308	1.1044	1.4963	1.5085	1.5451
④	1.2986	1.2962	1.2702	1.2626	1.3375	1.3446	1.3479
⑤	1.6031	1.5900	1.5740	1.5680	1.6732	1.6684	1.6681
⑥	1.2791	1.2780	1.2739	1.2753	1.3187	1.2799	1.1607

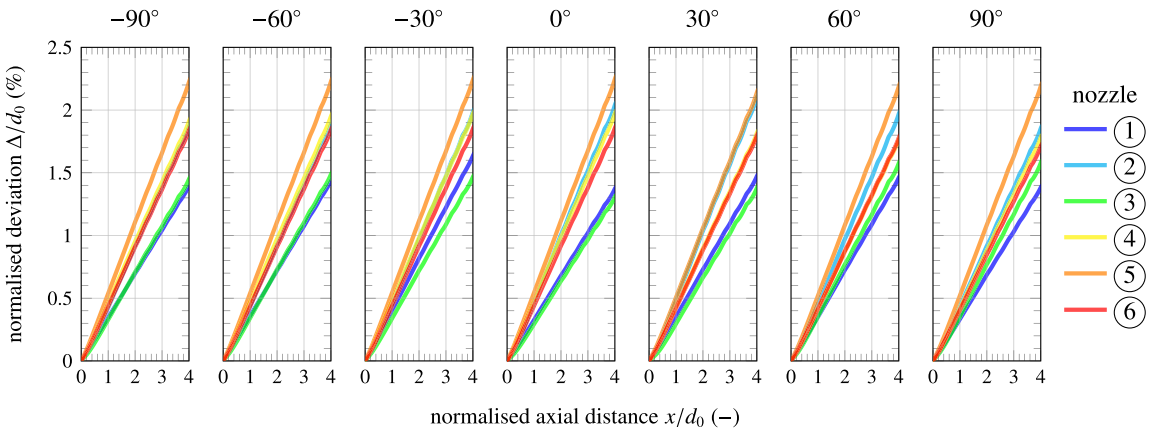

Fig. 6. The computed deviation of the water jet centreline to the needle axis is shown as the normalised distance for each nozzle and different penstock pipe bend configurations.

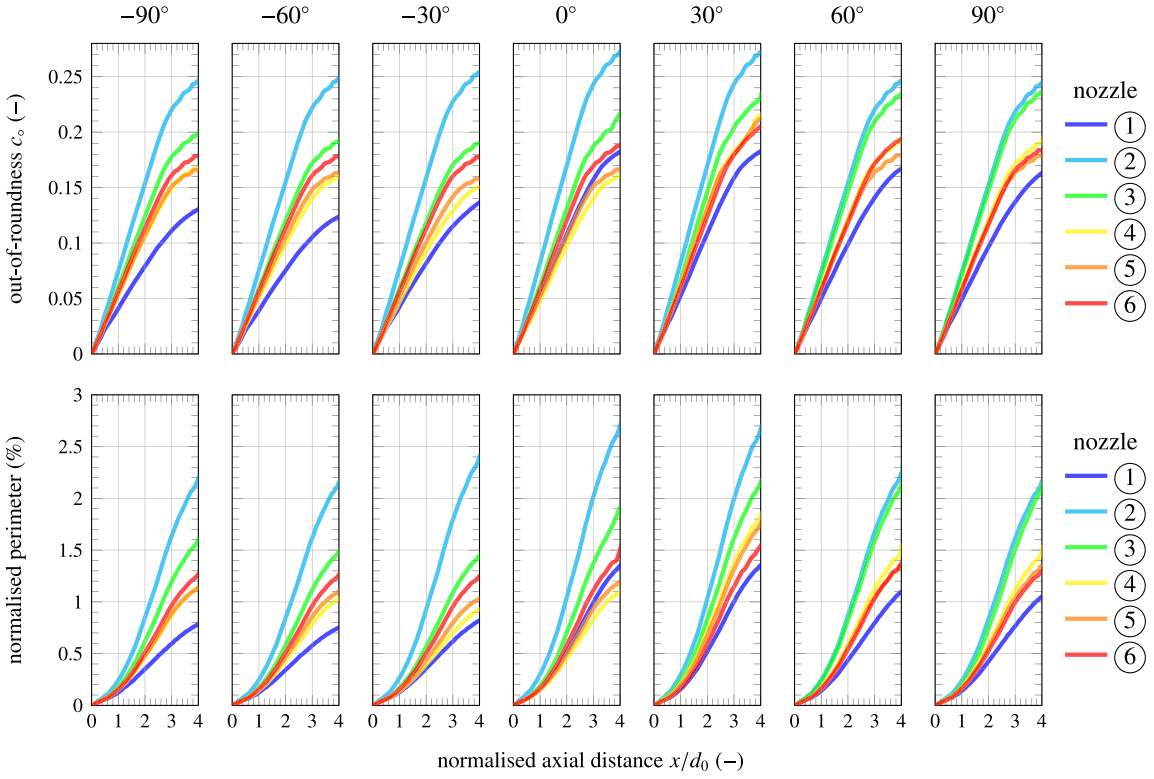

Fig. 7. The parameter out-of-roundness, $c_o = r_{max} - r_{min}/r_{theoretical}$, is shown in the upper row for the evaluation of the water jet shape for different pipe bend configurations. In the lower row, the water jet perimeters normalised by the circumference of the ideal circular water jet are plotted over the axial distance for different penstock pipe bend configurations.

Table 2
The secondary velocity magnitudes normalised by the primary flow velocity are evaluated at the station upstream of the needle body (the locations are illustrated in Fig. 3) for different penstock pipe bend configurations, where the values are presented in percent.

	−90°	−60°	−30°	0°	30°	60°	90°
①	7.2073	7.2377	7.0756	7.8772	7.8750	7.7492	7.6287
②	15.4605	15.3726	18.0969	17.7839	16.7787	14.4769	13.0687
③	11.7656	10.9477	10.6798	11.5375	16.0115	15.4394	15.4964
④	9.3973	9.1667	9.0652	9.0501	10.9834	10.9579	10.9286
⑤	9.3535	9.2159	9.0206	8.9403	10.7752	10.1459	10.1223
⑥	9.8274	9.7944	9.7480	9.6924	10.8232	10.8788	9.9513

the fourth and fifth nozzle is sometimes reversed, but the differences in the estimated values are marginal.

Comparing the relative amplitude pattern in Tables 1 and 2 reveals similarities, particularly for the first three nozzles. The free water jet deviation is caused by the forces acting on it. A control volume surrounding the water jet is sketched in blue in Fig. 8. Assuming that the water jet expands into free ambient conditions, there are no outer forces at boundaries other than at the nozzle exit and the central

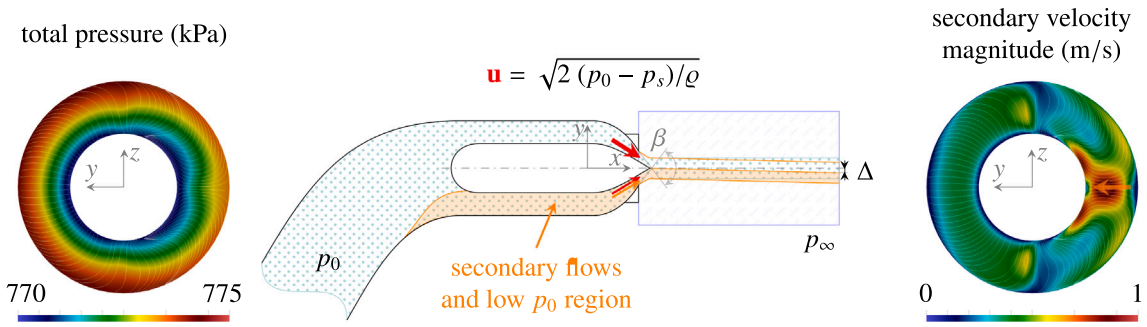

Fig. 8. The effect of the mass flow rate imbalance across the nozzle sides and the secondary flows on the free water jet deviation is sketched. The contour plots (total pressure to the left and secondary velocity magnitudes to the right) show the simulation data for the second nozzle without penstock pipe bend, where the plane's location is indicated through the coordinate system. The profiles holding the needle body are arranged in the z-direction, and therefore, the downstream wake is clearly visible. (For interpretation of the references to colour in this figure legend, the reader is referred to the web version of this article.)

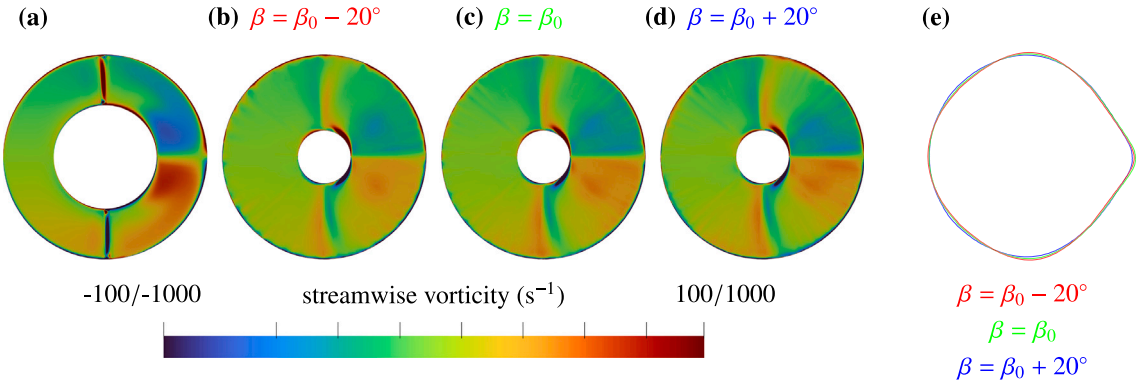

Fig. 9. The effect of the mouthpiece convergence angle, β, on the streamwise vorticity evolution and the free water jet deformation is illustrated, where the data shown represents the second nozzle without penstock pipe bend. Subfigure (a) shows the streamwise vorticity component in a plane just upstream of the nozzle convergence (which is the same plane as indicated in Fig. 8). The subfigures (b–d) show the streamwise vorticity component at the nozzle exit for different mouthpiece convergence angles. (The scale -100 s^{-1} to 100 s^{-1} applies for subfigure (a), while the values -1000 s^{-1} to 1000 s^{-1} apply for the subfigures (b–d).) Subfigure (e) compares the area-conserved free water jet shapes resulting at the distance of two nozzle exit diameters downstream from the exit.

spear. The nozzle's total pressure distribution is non-uniform, with higher flow velocities and static pressure on the outer curvature side (with corresponds to the left side looking towards the nozzle exit in the present investigation). Because $\mathbf{u} = \sqrt{2\,(p_0 - p_s)/\varrho}$ holds along a streamline without losses, with p_s being the local static pressure, p_∞ being the ambient pressure and p_0 being the total pressure in the nozzle, the flow velocities at the nozzle exit (i.e. $p_s \approx p_\infty$) are higher on one side than the other (see Fig. 8). The flow converges at the nozzle exit (given by the spear and mouthpiece angle), and the flow momentum over the axis is not balanced. Thus, the free water jet centreline deviates off the nozzle axis. Additionally, secondary flows due to the branch line curvature are present (see the right subfigure shown in Fig. 8), which can cause a radial flow momentum because of the flow recirculation in the centre. High secondary flow velocities can partially influence free water jet deviation by counteracting the effect of the mass flow rate imbalance across the nozzle sides. This effect can explain how high secondary velocity magnitudes listed in Table 2 compensate high mass flow rate imbalances across the nozzle sides shown in Table 1, which leads finally to the observed water jet deviation shown in Fig. 6.

The implications of these observations are worth noting, indicating how the two phenomena, i.e., mass flow rate imbalance across the nozzle and the secondary flows causing water jet deviation, can be influenced separately. The relative amplitude due to an imbalanced total pressure distribution over the nozzle is related to the differences in the total acting head (i.e. $\int \mathbf{u}_\pm^2 \varrho/2 dA = \int (p_{0,\pm} - p_s) dA$) at the nozzle exit. The final nozzle convergence angle shapes the nozzle exit, which governs the water ejection direction and, hence, also the deflecting force direction. The equations illustrate that the internal flow path provided by the spear and mouthpiece design has no impact on deflecting force direction due to imbalanced total pressure distributions. The evolution of the secondary flows through the nozzle is given by the incompressible vorticity transport equation,

$$\frac{D\boldsymbol{\omega}}{Dt} = \frac{\partial \boldsymbol{\omega}}{\partial t} + (\mathbf{u} \cdot \nabla)\boldsymbol{\omega} = (\boldsymbol{\omega} \cdot \nabla)\,\mathbf{u} + \nu \nabla^2 \boldsymbol{\omega}\,, \tag{7}$$

where $\boldsymbol{\omega}$ is the vorticity. The left-hand side represents the material derivative and thus describes the rate of change of vorticity of the moving fluid due to unsteadiness and convection. The last term on the right-hand side models the influence of the viscous forces on the vorticity transport, which can be assumed to be small because of the typically high Reynolds number flow. The first term on the right-hand side represents the vorticity stretching due to the flow velocity gradients, i.e. the amplification of vorticity caused by the flow acceleration in the nozzle, and contains partial spatial derivatives. Fig. 9 compares the contours of the streamwise vorticity component for different mouthpiece convergence angles, β, where the definition is sketched in Fig. 8. Because only the final slope of the outer nozzle contour differs by $\pm 20°$ for these cases, the streamwise vorticity contours are equal upstream of the nozzle convergence. Figs. 9 (b–d) show that the amplitude of the streamwise vorticity at the nozzle exit is influenced by the mouthpiece convergence angle, where a lower nozzle convergence angle decreases the streamwise vorticity component and a larger nozzle convergence angle increases the streamwise vorticity component. Fig. 9(e) illustrates that the amplitude of the streamwise vorticity component scales with the area-conserved free water jet shape deformation. Hence, the spear and mouthpiece design can influence the vorticity magnitude

at the nozzle exit through different physical mechanisms than the imbalance effect of the total pressure distribution over the nozzle. - A short mouthpiece, i.e. with high convergence angles, is optimal for a single nozzle with straight axial feed because the frictional losses are reduced to a minimum and other factors, such as secondary flows and total pressure imbalances over the nozzle, are negligible. With a pipe bend upstream of the nozzle, secondary flows and total pressure imbalances across the nozzle are crucial to the Pelton turbine efficiency, and high nozzle convergence angles become suboptimal, amplifying vorticity perturbations. These arguments can explain the experimental observations by other researchers, e.g. Petley et al. (2019).

4. Conclusions

The present work investigates the importance of the penstock in the distributor line optimisation process of Pelton turbines. Different pipe bends with commonly applied curvature radii are attached upstream of the Pelton turbine manifold with six nozzles. Numerical simulations are employed to analyse the effect on the multiphase flow in terms of water jet quality parameters, i.e. mass flow rate distribution, secondary flow structure generation, and water jet shape deformation, which are commonly applied for Pelton turbine manifold design and optimisation. The main conclusions are as follows;

- Even gentle pipe bends in the upstream piping system affect the impulse direction of the flow entering the manifold. The direction of high-momentum inflow changes the redistribution in the manifold particularly.
- The penstock piping changes velocity distribution at the branch line junctions, and thus, the secondary flows upstream of the nozzles evolve differently. Even pipe bends of 30° are found to cause flow changes of decisive impact on the secondary flows and the free water jet deformation.
- Although the secondary flow structures upstream of the nozzle are altered with different pipe bends upstream of the manifold, the link to the water jet deformation is not straightforward. Nonetheless, the secondary flow ratio is found to govern the free water jet deformation and is a good estimator.
- The mass flow rate imbalance across the nozzle sides affects the water jet deviation, but the secondary flows also influence this quality parameter. - Secondary flows can counterbalance mass flow rate imbalances, reducing the expected water jet deviation.

It may be remarked that the above observations have been made for a particular manifold and nozzle design and low-head operating conditions. Further, flow simulations, including the Pelton turbine runner, are required to rate the impact of the penstock piping in efficiency points, which are suggested for future work.

CRediT authorship contribution statement

Bernhard Semlitsch: Writing – review & editing, Writing – original draft, Visualization, Validation, Software, Resources, Methodology, Investigation, Formal analysis, Data curation, Conceptualization.

Declaration of competing interest

The authors declare that they have no known competing financial interests or personal relationships that could have appeared to influence the work reported in this paper.

Data availability

The data that has been used is confidential.

Acknowledgment

The authors acknowledge TU Wien Bibliothek for financial support through its Open Access Funding Programme.

References

Chongji, Z., Yexiang, X., Wei, X., Tao, W., Jin, Z., Zhengwei, W., Yongyao, L., 2016. Numerical analysis of pelton nozzle jet flow behavior considering elbow pipe. In: IOP Conference Series: Earth and Environmental Science. Vol. 49, (2), IOP Publishing, 022005. http://dx.doi.org/10.1088/1755-1315/49/2/022005.

Deng, H., Song, K., Deng, F., Huang, Y., Luo, T., Zhou, Y., Qin, B., Zeng, Y., Yu, Z., Pang, J., Liu, X., 2023. Nozzle jet deviation from bucket pitch circle's effect on the stability and efficiency of pelton turbine. Processes 11 (5), http://dx.doi.org/10.3390/pr11051342.

Fiereder, R., Riemann, S., Schilling, R., 2010. Numerical and experimental investigation of the 3D free surface flow in a model pelton turbine. In: IOP Conference Series: Earth and Environmental Science. Vol. 12, (1), IOP Publishing, 012072. http://dx.doi.org/10.1088/1755-1315/12/1/012072.

Giesecke, J., Mosonyi, E., 2009. Wasserkraftanlagen: Planung, Bau und Betrieb. Vol. 5, Springer-Verlag.

Hahn, F.J.J., Semlitsch, B., Bauer, C., 2022. On the numerical assessment of flow losses and secondary flows in Pelton turbine manifolds. In: IOP Conference Series: Earth and Environmental Science. Vol. 1079, (1), IOP Publishing, 012082. http://dx.doi.org/10.1088/1755-1315/1079/1/012082.

Han, L., Duan, X., Gong, R., Zhang, G., Wang, H., Wei, X., 2019. Physic of secondary flow phenomenon in distributor and bifurcation pipe of Pelton turbine. Renew. Energy 131, 159–167. http://dx.doi.org/10.1016/j.renene.2018.06.116.

Jošt, D., Mežnar, P., Lipej, A., 2010. Numerical prediction of Pelton turbine efficiency. In: IOP Conference Series: Earth and Environmental Science. Vol. 12, (1), IOP Publishing, 012080. http://dx.doi.org/10.1088/1755-1315/12/1/012080.

Jošt, D., Škerlavaj, A., Pirnat, V., Morgut, M., Nobile, E., 2019. Numerical prediction of efficiency and cavitation for a Pelton turbine. In: IOP Conference Series: Earth and Environmental Science. Vol. 240, (6), IOP Publishing, 062033. http://dx.doi.org/10.1088/1755-1315/240/6/062033.

Kumashiro, T., Alimirzazadeh, S., Maertens, A., Jahanbakhsh, E., Leguizamón, S., Avellan, F., Tani, K., 2019. Numerical investigation of the jet velocity profile and its influence on the Pelton turbine performance. In: IOP Conference Series: Earth and Environmental Science. Vol. 240, (7), IOP Publishing, 072006. http://dx.doi.org/10.1088/1755-1315/240/7/072006.

Mack, R., Gola, B., Smertnig, M., Wittwer, B., Meusburger, P., 2014. Modernization of vertical Pelton turbines with the help of CFD and model testing. In: IOP Conference Series: Earth and Environmental Science. Vol. 22, (1), IOP Publishing, 012002. http://dx.doi.org/10.1088/1755-1315/22/1/012002.

Mack, R., Rohne, W., Riemann, S., Knapp, W., Schilling, R., 2006. Using the potential of CFD for Pelton turbine development. In: 23rd IAHR Symposium on Hydraulic Machinery and Systems. Yokohama, Japan.

Patel, K., Patel, B., Yadav, M., Foggia, T., 2010. Development of pelton turbine using numerical simulation. In: 25th IAHR Symposium on Hydraulic Machinery and Systems, Timisoara, Romania.

Peron, M., Parkinson, E., Geppert, L., Staubli, T., 2008. Importance of jet quality on pelton efficiency and cavitation. In: International Conference on Hydraulic Efficiency Measurements, Milan, Italy, Sept. pp. 3–6.

Petley, S., Židonis, A., Panagiotopoulos, A., Benzon, D., Aggidis, G.A., Anagnostopoulos, J., Papantonis, D., 2019. Out with the old, in with the new: Pelton hydro turbine performance influence utilizing three different injector geometries. J. Fluids Eng. 141 (8), http://dx.doi.org/10.1115/1.4042371.

Riemann, S., 2009. Untersuchung der instationären Strömung in einer Peltonturbine (Ph.D. thesis). Technische Universität München.

Sadlo, F., Peikert, R., Parkinson, E., 2004. Vorticity based flow analysis and visualization for pelton turbine design optimization. In: IEEE Visualization 2004. IEEE, pp. 179–186. http://dx.doi.org/10.1109/VISUAL.2004.128.

Sandmaier, L., Meusburger, P., Benigni, H., 2023. Transient 3D CFD simulation of a pelton turbine—A state-of-the-art approach for pelton development and optimisation. Int. J. Turbomach., Propul. Power 8 (1), 10. http://dx.doi.org/10.3390/ijtpp8010010.

Santolin, A., Cavazzini, G., Ardizzon, G., Pavesi, G., 2009. Numerical investigation of the interaction between jet and bucket in a Pelton turbine. Proc. Inst. Mech. Eng. A 223 (6), 721–728. http://dx.doi.org/10.1243/09576509JPE824.

Staubli, T., Abgottspon, A., Weibel, P., Bissel, C., Parkinson, E., Leduc, J., Leboeuf, F., 2009. Jet quality and Pelton efficiency. In: Hydro, Lyon, France, Oct 26-28.

Staubli, T., Bissel, C., 2009. Final report jet improvement for swiss pelton plants. Tech. rep., swiss electric research.

Unterberger, P., Bauer, C., Gaschl, J., Mack, R., 2010. Studies on the free jet of Pelton nozzles. In: Proceedings of the 16th International Seminar on Hydropower Plants, Wien, Austria.

Zeng, C., Xiao, Y., Luo, Y., Zhang, J., Wang, Z., Fan, H., Ahn, S.-H., 2018. Hydraulic performance prediction of a prototype four-nozzle Pelton turbine by entire flow path simulation. Renew. Energy 125, 270–282. http://dx.doi.org/10.1016/j.renene.2018.02.075.

Zhang, Z., Casey, M., 2007. Experimental studies of the jet of a Pelton turbine. Proc. Inst. Mech. Eng. A 221 (8), 1181–1192. http://dx.doi.org/10.1243/09576509JPE408.